## TECHNICAL ARTICLE

# Micromechanical Fields Associated with Irregular Deformation Twins in Magnesium

Brandon Leu, M. Arul Kumar, Paul F. Rottmann, Kevin J. Hemker, and Irene J. Beyerlein

Submitted: 28 December 2021 / Revised: 28 June 2022 / Accepted: 20 July 2022

Understanding and controlling the development of deformation twins is paramount for engineering strong and stable hexagonal close-packed (HCP) Mg alloys. Actual twins are often irregular in boundary morphology and twin crystallography, deviating from the classical picture commonly used in theory and simulation. In this work, the elastic strains and stresses around irregular twins are examined both experimentally and computationally to gain insight into how twins develop and the microstructural features that influence their development. A nanoprecession electron diffraction (N-PED) technique is used to measure the elastic strains within and around a {1012} tensile twin in AZ31B Mg alloy with nm scale resolution. A full-field elasto-viscoplastic fast Fourier transform (EVP-FFT) crystal plasticity model of the same sub-grain and irregular twin structure is employed to understand and interpret the measured elastic strain fields. The calculations predict spatially resolved elastic strain fields in good agreement with the measurement, as well as all the stress components and the dislocation density fields generated by the twin, which are not easily obtainable from the experiment. The model calculations find that neighboring twins, several twin thicknesses apart, have little influence on the twin-tip micromechanical fields. Furthermore, this work reveals that irregularity in the twin-tip shape has a negligible effect on the development of the elastic strains around and inside the twin. Importantly, the major contributor to these micromechanical fields is the alignment of the twinning shear direction with the twin boundary.

**Keywords** crystal plasticity, deformation twin, local strain, magnesium, N-PED

## 1. Introduction

Twinning is an important mode of plastic deformation in low crystal-symmetry materials, particularly hexagonal close-packed (HCP) metals, such as Zr, Mg, and Ti (Ref 1, 2). Deformation twins form first by nucleating twin embryos where suitable defects and stresses are present (Ref 3), mostly at grain boundaries (Ref 4), and then developing them into thin lamellae by propagation of the twin tip (Ref 5), and finally expanding the lamellae via twin boundary migration (Ref 6-10). This step-

This invited article is part of a special topical focus in the *Journal of Materials Engineering and Performance on Magnesium*. The issue was organized by Prof. C. (Ravi) Ravindran, Dr. Raja Roy, Mr. Payam Emadi, and Mr. Bernoulli Andilab, Ryerson University.

Brandon Leu, Department of Mechanical Engineering, University of California Santa Barbara, Santa Barbara, CA 93106, USA; M. Arul Kumar, Materials Science and Technology Division, Los Alamos National Laboratory, Los Alamos, NM 87545, USA; Paul F. Rottmann, Department of Chemical and Materials Engineering, University of Kentucky, Lexington, KY 40506, USA; Kevin J. Hemker, Department of Mechanical Engineering, John Hopkins University, Baltimore, MD 21218, USA; Irene J. Beyerlein, Department of Mechanical Engineering, University of California Santa Barbara, Santa Barbara, CA 93106, USA; and Department of Materials, University of California Santa Barbara, Santa Barbara, CA 93106, USA. Contact e-mail: beyerlein@engineering.ucsb.edu.

by-step process produces a three-dimensional (3D) volumetric twin domain with an abrupt lattice reorientation with respect to the parent crystal and localized shear. For instance, the  $\{10\overline{1}2\}$  tensile twin in Mg reorients the crystal by  $86.3^{\circ}$  and imposes a 12.9% characteristic shear (Ref 2). Consequently, heterogeneous micromechanical fields within and around the twin domains in the surrounding crystal are generated (Ref 6, 11-14). Accurate evaluation of the stress and strain fields at the twin tip and around the twin boundaries can provide insight into how twins develop after formation and affect the macroscopic deformation response (Ref 2, 6, 15).

Various experimental techniques are used to measure the stress/strain fields, including surface techniques, such as highresolution electron backscatter diffraction (HR-EBSD) with digital image correlation (DIC), as well as nondestructive techniques, like 3D x-ray diffraction (3D-XRD). HR-EBSD with DIC is able to measure strain on the sample surface with approximately 50 nm spatial resolution and an error of 10<sup>-4</sup> (Ref 12). 3D-XRD is able to acquire spatially resolved micromechanical fields in the interior of the sample with  $\sim$ 1  $\mu$ m resolution and an error of 10<sup>-3</sup> (Ref 14). On the other hand, x-ray synchrotron with the differential aperture x-ray microscopy (DAXM) technique can obtain spatially resolved stress/strain fields from the interior of the sample with  $\sim$  250 nm resolution and errors of 10<sup>-4</sup> (Ref 13). Although these techniques have successfully measured the stress/strain fields associated with the twins, the spatial resolution is insufficient for understanding the twinning processes at twin boundaries and twin tips, which have facets/interfaces a few nm in length (Ref 8, 10, 16, 17). To overcome this issue, high-resolution transmission electron microscopy (HR-TEM) with nanobeam

Published online: 15 August 2022

electron diffraction (NBED) method has been employed to map the elastic strain fields around a twin domain with a spatial resolution of  $\sim\!0.2$  nm and an error of  $\sim\!6\times10^{-3}$  (Ref 18). However, the elastic strain suggested by this technique is up to 10% in a relatively large region, far beyond the material elastic strain limit. These elastic strain fields are unrealistically high. Recently, the nanoelectron precession diffraction (N-PED) technique has been shown to obtain realistic elastic strain fields with a spatial resolution of a few nm (Ref 19, 20). It has been successfully employed to map the elastic strain fields near the grain boundaries in boron carbide and dislocations in magnesium (Ref 19, 20). In this work, this N-PED technique is employed to measure the elastic strains within and around  $\{10\overline{1}2\}$  tensile twin domains in HCP magnesium.

The grain microstructure of a polycrystalline material can be heterogeneous and the twin morphology can be complex (Ref 21-24), making it difficult to deconvolute the source for the heterogeneity in the experimentally measured strain fields. It is unclear whether the measured strain fields are primarily governed by the intrinsic twinning shear process or twin morphology or by the interaction of twins with other microstructural features. In turn, it is almost impossible to develop a comprehensive understanding of deformation twins from experimentally measured stress or strain fields alone. To address this, a spatially resolved elasto-viscoplastic fast Fourier transform (EVP-FFT) model (Ref 25) is combined with the N-PED technique. Specifically, the EVP-FFT model is employed to identify the features of the twin responsible for the measured heterogeneous strain fields in and around the twin domains. First, the experimentally observed twinned crystal is simulated, and the model calculated strain fields are compared with N-PED measurements. The model predicts the twin-induced stresses and defect distributions that arise solely from the intrinsic twinning shear transformation, without the influence of external loads and nearby twins, which are difficult to fully characterize and account for. Furthermore, through a systematic investigation, the respective roles of the geometry of the twin, alignment of the twinning shear direction with the twin boundary, and the presence of neighboring twins on the development of elastic strains are analyzed.

The paper is structured as follows. The experimental details such as material, initial loading, strain mapping technique are presented in Sect. 2. Section 3 briefly describes the EVP-FFT framework for modeling twins explicitly. Measured and calculated elastic strain fields are presented in Sects. 4.1 and 4.2, respectively. The calculated dislocation density fields ahead of the twin in the surrounding crystal are discussed in Sect. 4.3. In Sects. 4.4 and 4.5, the effect of neighboring twins and twin morphology on the elastic strain fields is explored computationally. The main conclusions on the extent to which twin boundary irregularity and nearby twin structures affect the twin-tip fields and possible growth are given in Sect. 5.

## 1.1 Experiments: Strain Mapping Using N-PED

A polycrystalline AZ31B magnesium alloy comprised of several hundred-micron size equiaxed grains was examined in this study. The initial texture of the material was found to have basal texture. The sample was compressed in the rolling direction to 2% engineering strain (Ref 20, 26-28). A section of the compressed sample was electropolished to electron transparency, enabling observation of the microstructure, which

contained numerous lenticular twins terminating within grain interiors. A staggered array of twins was located, see Fig. 1a, and tilted such that a  $[11\overline{2}0]$  direction for both the parent grain and twin was aligned with the beam direction. The specimen was imaged using a Philips CM200 TEM operated at 200 kV with a 10-µm condenser aperture, creating a nearly parallel beam and diffraction spots rather than disks. The microscope was operated in TEM mode with the beam location and precession controlled by an external DigiSTAR unit. Spot diffraction patterns were recorded from a 2.5 µm×2.7 µm region with a 10 nm step size, 4 nm beam size, 0.8° precession angle, and an exposure time of approximately 20 ms for each diffraction pattern. Using these diffraction patterns, a digital aperture was placed over the central spot to generate a virtual brightfield scanning transmission electron microscope (STEM) image that reveals diffraction contrast in the region, seen in Fig. 1a. Figure 1b shows an orientation map of the same region highlighting the abrupt change of in-plane orientation across the twin boundary. The observed twins are irregular in two ways. Firstly, they have unique morphologies, with rough twin boundaries that deviate from the  $\{10\overline{1}2\}$  twin boundary plane. Secondly, the long dimension of the twin (most likely the propagation direction) is misaligned from the twinning shear direction by  $\sim 23^{\circ}$ .

To calculate the elastic strain fields surrounding and within the irregular twins, a high-resolution scan with a step size of 4 nm was recorded in the region identified in Fig. 1b. Using the TOPSPIN software (NanoMEGAS) (Ref 29), the relative 2D elastic strain fields were calculated in the parent crystal surrounding the twin using a reference diffraction pattern from the location marked in Fig. 2. The reference location is selected in such a way that the diffraction pattern at that point would not be affected by the twins and thus can represent the un-twinned strained parent crystal. To calculate the elastic strains within the twin, a reference diffraction pattern is taken from the center of the twin, shown in Fig. 3. The reference point is ~80 nm from the twin boundaries.

## 2. Numerical Methods

## 2.1 EVP-FFT Formulation

Spatially resolved elasto-viscoplastic fast Fourier transform (EVP-FFT)-based crystal plasticity model is used to explicitly simulate the formation of twins and predict the elastic strain fields within and around the twins. The EVP-FFT model was initially developed by Lebensohn et al. as a tool to compute the micromechanical fields of polycrystalline metals (Ref 25). Since then, the model has been extended to study the deformation twinning in single-phase materials (Ref 30), multi-phase material systems (Ref 31, 32), twin-twin interactions (Ref 33), and free surface effects (Ref 34). The model allows for the prediction of internal stresses and strains with an intragranular resolution to aid in the interpretation of spatially resolved measurements. In what follows, the EVP-FFT formulation is briefly presented here.

The EVP-FFT model is built upon a periodic square grid of discrete voxels. The stresses,  $\sigma(x)$ , at each material point, x, are related to the elastic strains,  $\varepsilon^e(x)$ , by a time-discretized Hooke's law:

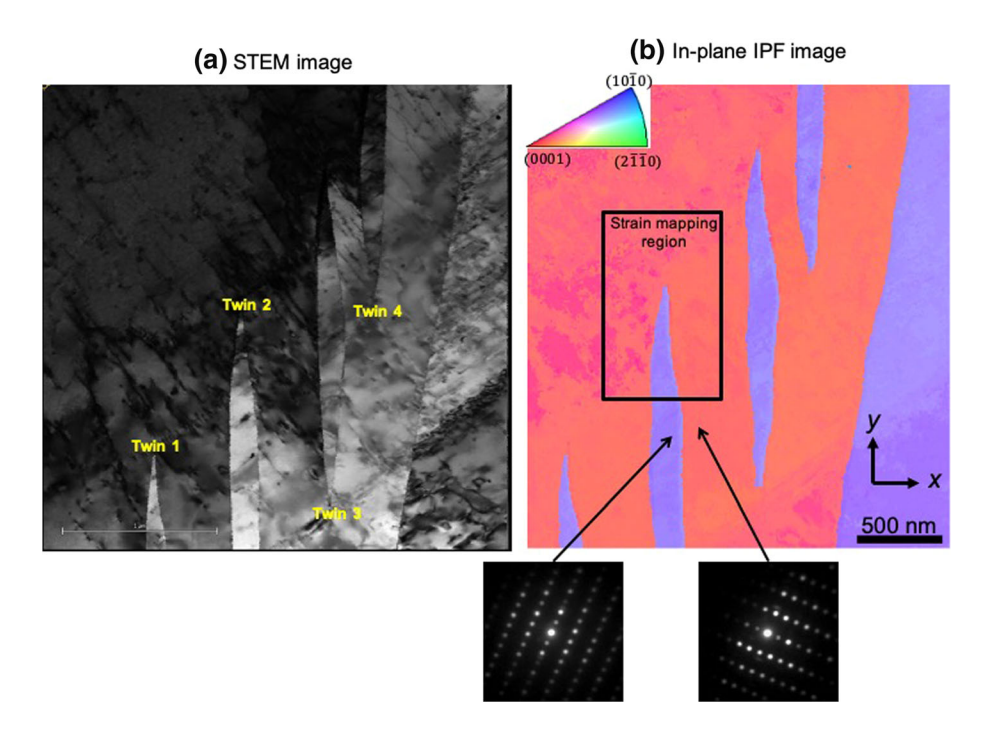


**Fig. 1** (a) Virtual brightfield STEM image and (b) orientation map of part of the deformed microstructure show the formation of multiple parallel  $\{10\overline{1}2\}$  tensile twins. The color scheme in the orientation map follows the standard stereographic triangle with respect to in-plane direction. Twin 2 is selected for elastic strain mapping, and the region is marked in (b)

$$\sigma^{t+\Delta t}(x) = C(x) : \varepsilon^{e,t+\Delta t}(x)$$
 (Eq 1)

In the above, C(x) is the elastic stiffness tensor and the superscripts indicate an increment in time, t, by an amount  $\Delta t$ . The total strain tensor  $\varepsilon(x)$  is equal to the sum of the elastic strain and the plastic strain tensor. In the present work, the latter is comprised of plastic strain due to slip,  $\varepsilon^p(x)$ , and the homogenous twin shear transformation strain,  $\varepsilon^{tw}(x)$ , in the twin domain. Accordingly, the elastic strain,  $\varepsilon^e(x)$ , is given by

$$\varepsilon^{e,t+\Delta t}(x) = \varepsilon^{t+\Delta t}(x) - \varepsilon^{p,t}(x) - \dot{\varepsilon}^{p,t+\Delta t}(x)\Delta t - \varepsilon^{tw,t}(x) - \Delta \varepsilon^{tw}(x)$$
(Eq 2)

where  $\dot{e}^p(x)$  is constitutively related to the stress through a sum over the N active slip systems that the user defines.  $\dot{e}^p(x)$  is written as:

$$\dot{\varepsilon}^p(x) = \sum_{s=1}^N m^s(x) \dot{\gamma}^s(x) = \dot{\gamma}_0 \sum_{s=1}^N m^s(x) \left( \frac{|m^s(x):\sigma(x)|}{\tau_c^s(x)} \right)^n \mathrm{sgn}(m^s(x):\sigma(x))$$
 (Eq 3)

In the above, the Schmid tensor,  $m^s$ , is the symmetric part of  $(b^s \otimes n^s)$ , where  $b^s$  and  $n^s$  are the unit vectors along the slip direction and the slip plane normal, respectively, of slip system s. The strength  $\tau_c^s(x)$  is the critical resolved shear stress (CRSS) needed to activate slip system s,  $\dot{\gamma}_o$  is a normalization factor and n is the stress exponent. A twin domain is identified a priori in the crystal. Uniformly across the domain, the characteristic shear strain associated with the twin is reached by incrementing the strain,  $\Delta e^{tw}(x)$ , as follows:

$$\Delta \varepsilon^{tw}(x) = \frac{S^{tw}}{N^{tw}} \tag{Eq 4}$$

where  $S^{\text{tw}}$  is the characteristic twin shear of the material, and  $N^{\text{tw}}$  is the user-defined number of twin strain increments, which is kept sufficiently large to ensure convergence. The strain tensors  $\varepsilon^{\text{tw}}$  and  $\Delta \varepsilon^{\text{tw}}$  are null outside of the twin domain.

## 2.2 Dislocation Density-Based Hardening Law

Following the dislocation density (DD)-based hardening law, the CRSS,  $\tau_s^s(x)$  for each slip system, s, is evolved as a function of strain rate and temperature (Ref 35). Below we provide a brief summary and for more details, refer the reader to (Ref 35).

The resistance to slip is determined through a sum of multiple factors and is written as:

$$\tau_c^s = \tau_0^s + \tau_{\text{debris}}^s + \tau_{\text{forest}}^s$$
 (Eq 5)

The Peierls stress,  $\tau_0^s$ , represents the initial slip resistance of slip system s and is dependent on the initial dislocation density and intrinsic material properties. The scalar resistance  $\tau_{\text{debris}}^s$  is due to arrays of dislocation substructures and scales according to (Ref 36):

$$\tau_{\rm debris}^s = K \mu b^s \sqrt{\rho^{\rm debris}} \log \frac{1}{b^s \sqrt{\rho^{\rm debris}}}$$
 (Eq 6)

where K is a numerical constant equal to 0.086 (Ref 36, 37),  $b^s$  is the Burgers vector,  $\mu$  is the shear modulus, and  $\rho^{\text{debris}}$  is the total debris dislocation density. The density  $\rho^{\text{debris}}$  is calculated through the sum of debris contributed by each slip system:

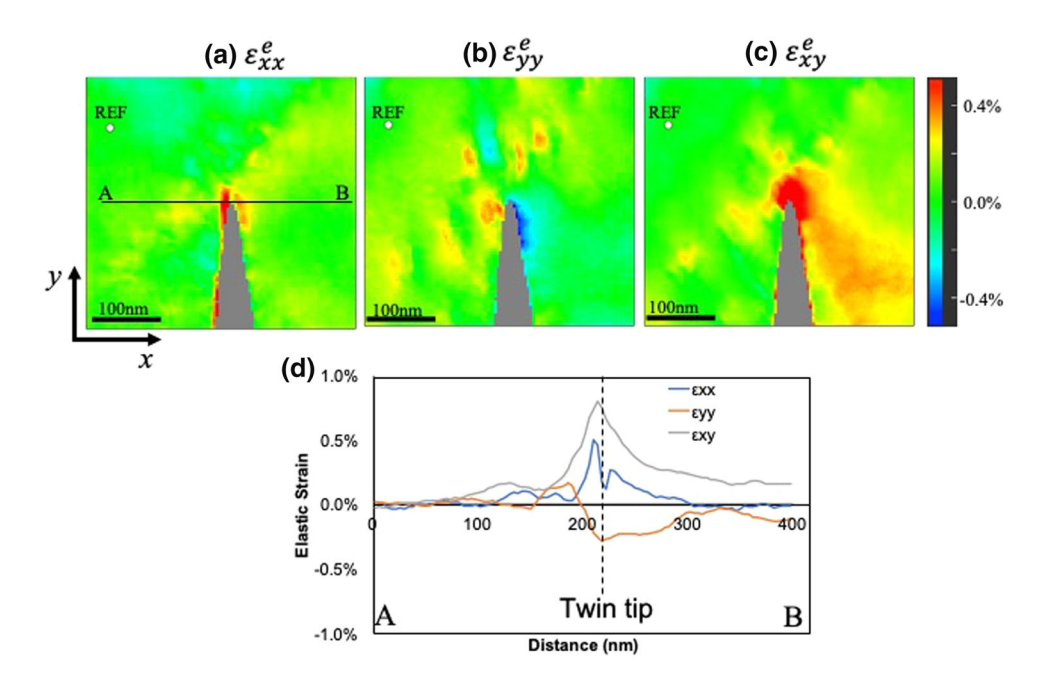


Fig. 2 Experimentally measured elastic strains of (a)  $\varepsilon_{xx}^e$ , (b)  $\varepsilon_{yy}^e$ , and (c)  $\varepsilon_{xy}^e$  fields around the twin tip. (d) Elastic strain profile along line A-B (shown in (a)) ahead of the twin tip

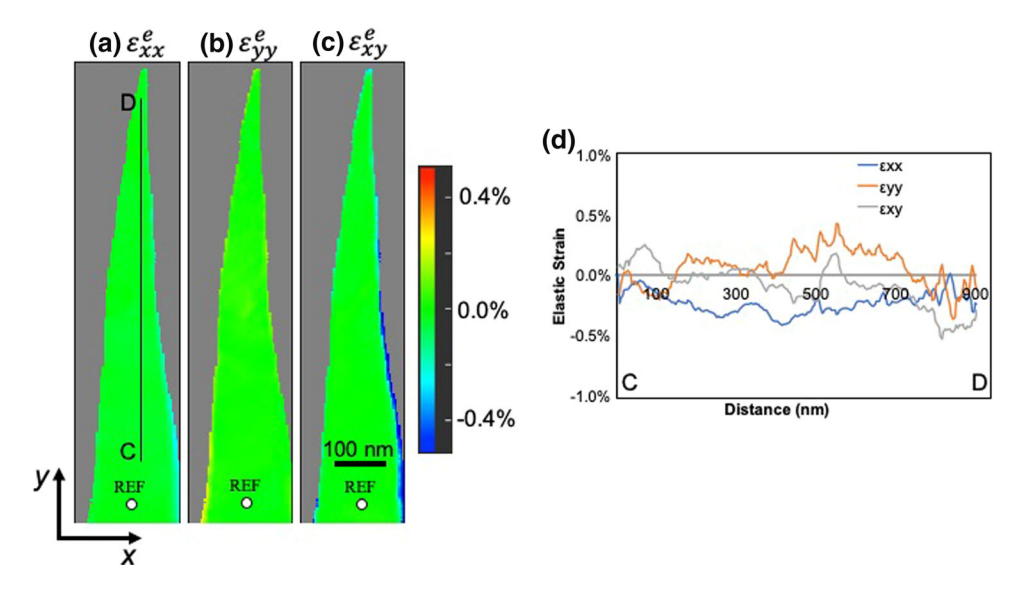


Fig. 3 Experimentally measured elastic strains of (a)  $\varepsilon_{xx}^e$ , (b)  $\varepsilon_{yy}^e$ , and (c)  $\varepsilon_{xy}^e$  fields inside the twin domain. (d) Elastic strain profile along the line C-D (shown in (a)), which is parallel to the long axis of the twin

$$\partial \rho_{\rm debris} = q \sum_s f^s \frac{\partial \rho^s_{\rm rem}}{\partial \gamma^\alpha} {\rm d} \gamma^s \tag{Eq 7}$$

In the above, q is the rate coefficient for how debris accumulates and set to 4 in this work. The density  $\rho_{\text{rem}}^s$  is the remnant dislocation density of each slip system that contributes to the formation of debris.  $f^s$  is a term that describes debris dislocation storage rates, which increases with the amount of debris collected as:

$$f^s = A^s b^s \sqrt{\rho^{\text{debris}}}$$
 (Eq 8)

where  $A^s$  is a temperature-dependent constant that describes how dislocation-dislocation interactions lead to the generation of debris. Lastly,  $\tau_{\text{forest}}^s$  represents the resistance to slip due to arrays of forest dislocations that block dislocation glide and scales as (Ref 38, 39):

$$\tau_{\text{forest}}^s = \chi \mu b^s \sqrt{\rho^s} \tag{Eq 9}$$

Here  $\chi$  is a dislocation interaction coefficient and is set to 0.9. In this work, dislocations of slip system mode, such as basal, prismatic, or pyramidal, can only be hardened by forest dislocations from the same type. The stored forest dislocation densities evolve via a competition between dislocation generation term with coefficient  $k_1^s$  that describes the trapping of gliding dislocations by forest dislocations and a thermally controlled annihilation term that represents the dynamic recovery of stored dislocations (Ref 27, 40, 41), i.e.,

$$\frac{\partial \rho^s}{\partial \gamma^s} = k_1^s \sqrt{\rho^s} - k_2^s (\dot{\epsilon}, T) \rho^s \tag{Eq 10}$$

where the coefficient on the dynamic recovery  $k_2^s$  is given by:

$$\frac{k_2^s}{k_1^s} = \frac{\chi b^s}{g^s} \left( 1 - \frac{kT}{D^s b^3} \ln \frac{\dot{\varepsilon}}{\dot{\varepsilon}_0} \right) \tag{Eq 11}$$

where k,  $\dot{\varepsilon}$ ,  $\dot{\varepsilon}_0$ ,  $D^s$ , and  $g^s$  are Boltzmann's constant, the strain rate at each voxel, a reference strain rate (set to be  $10^7$  1/s), a drag stress, and a normalized activation energy of slip system s.

#### 2.3 Model Setup

The experimentally obtained STEM micrograph shown in Fig. 1 is digitized into a 375 × 350 voxel simulation cell, for use as the initial microstructure, so that the model surface microstructure exactly mirrors the observed one. Since the subsurface structure is not known and we employ periodic boundary conditions, a columnar microstructure is adopted with the thickness of 6 voxels in the Z-direction. To minimize the effect of periodicity and image forces, the crystal is encased in the x-y plane in a 50-voxel thick homogeneous layer, which approximates the response of polycrystalline Mg.

The STEM technique provided crystallographic orientations for the entire microstructure is used. The average crystallographic orientations of the parent grain and twin domains are  $(156^{\circ}, 95^{\circ}, 267^{\circ})$  and  $(69^{\circ}, 85^{\circ}, 86^{\circ})$ , respectively, in the Bunge convention. The twin variant is identified to be  $(0\overline{1}12)[01\overline{1}1]$ , with both the twin plane normal and twin shear direction lying within the x-y plane. The twinning shear direction is oriented  $23.05^{\circ}$  counter-clockwise from the +y direction and the twin plane normal lies  $22.90^{\circ}$  counter-clockwise from the +x direction. As such, no strain gradients from the twin are expected in the z direction and the strain and stress fields of interest lie in the x-y plane.

As mentioned in Sect. 3.1, deformation at every voxel is accommodated by anisotropic elasticity and viscoplasticity. The anisotropic elastic coefficients of pure Mg, in GPa, used in the

calculations are:  $C_{11}$ =59.75,  $C_{12}$ =23.24,  $C_{13}$ =21.70,  $C_{33}$ =61.70, and  $C_{44}$ =17.0 (Ref 42). Viscoplasticity is assumed to be accommodated by crystallographic slip, with the following modes made available: basal  $\langle a \rangle$ :  $\{0001\}\langle 11\overline{2}0 \rangle$ , prismatic  $\langle a \rangle$ :  $\{10\overline{1}0\}\langle 11\overline{2}0 \rangle$ , and pyramidal  $\langle c+a \rangle$ :  $\{\overline{11}22\}\langle \overline{11}23 \rangle$  slip. The initial CRSS for these three modes and the associated DD-hardening law parameters are taken from (Ref 43) and listed in Table 1.

Deformation twinning is initiated from an unloaded state to capture the strain fields that develop purely from the formation of the twins, without the effects of any arbitrary loading. Twinning occurs through the incremental development of the characteristic twinning shear, 12.9% for the  $\{10\overline{1}2\}$  tensile twin in pure Mg (Ref 1). After the twin has fully developed, the upper three z-layers of the simulation cell are virtually removed to create a free surface (Ref 34). This step is accomplished by setting the material properties of those layers to be an isotropic linear elastic material that is extremely compliant with a Young's modulus of 1 MPa, intended to approximate the response of a vacuum. The simulation cell is then allowed to relax to a new energetic minimum. The resulting micromechanical fields are expected to be closer in approximation to those obtained experimentally through surface techniques (Ref 34). In all cases presented below, the calculated strain fields after free surface relaxation are then compared with the measured ones.

## 3. Results and Discussion

Initially, we focus our attention on the development of a single twin, labeled "twin 2" in Fig. 1a, without the influence of the neighboring twins. Later, we study the combined effects of all the twins seen in Fig. 1.

## 3.1 Experimentally Measured Elastic Strain Fields Associated with a Twin

The elastic strain fields around the twin tip were measured utilizing the N-PED technique described in Sect. 2. The reference point used for the elastic strain calculations surrounding the twin tip is marked in Fig. 2. From the measured strain fields shown in the top row, it is observed that tensile  $\varepsilon_{xx}^e$  strains develop on both sides of the twin tip, while the  $\varepsilon_{yy}^e$  strains are tensile on the left and compressive on the right side of the tip. Large elastic shear strains  $\varepsilon_{xy}^e$  are concentrated in a small region ahead of the twin tip. Furthermore, the shear strains in the region to the right of the twin tip are around 0.3%,

Table 1 Pure Mg dislocation density-based hardening law parameters were taken from (Ref 43)

	α=1 Prismatic (a)	α=2 Basal (a)	α=3 Pyramidal 1 (c+a)
$\tau_0^{\alpha}$ [MPa]	35.7	3.33	86.2
$b^{\alpha}$ [m]	3.231e-10	3.231e-10	6.0771e-10
$\varepsilon_{0}$ [1/s] $\rho_{0}$ [1/m <sup>2</sup> ] $\rho_{debris}$ [1/m <sup>2</sup> ] $A_{293K}^{\alpha}$ $k_{1}^{\alpha}$ [1/m] $g_{\alpha}^{\alpha}$	1.0e+07	1.0e+07	1.0e+07
$\rho_0 [1/m^2]$	1.50e+12	1.50e+12	1.50e+12
$\rho_{\text{debris}} [1/\text{m}^2]$	1.0e-01	1.0e-01	1.0e-01
$A_{293K}^{\alpha}$	0	0	0
$k_1^{\alpha}$ [1/m]	8.0e+09	6.7e+09	7.18e+09
$g^{\dot{\alpha}}$	3.36e-03	3.36e-03	3.36e-03
$D^{\alpha}$ [MPa]	7.98e+03	0.6e+03	24.33e+03

while a relatively strain-free region exists to the left side of the twin tip. It should be noted that the deformation history of the sample, specifically in the local region investigated in this study, is unknown, and the build-up of dislocation substructures in the grain could influence the strain measurement.

Figure 2(d) shows the elastic strains measured along line A-B that runs across the twin tip in the parent matrix. Strains  $\varepsilon_{xx}^e$ ,  $\varepsilon_{xy}^e$ , and  $\varepsilon_{xy}^e$  are plotted in blue, orange, and gray, respectively. The elastic strain line profiles reveal that the localized strain concentrations ahead of the twin tip for the  $\varepsilon_{xx}^e$  and  $\varepsilon_{xy}^e$  components reach 0.5% and 0.8%, respectively. In comparison with other nm-scale strain field measurements techniques, such as nanobeam electron diffraction (NBED) (Ref 18), the measured strains in Fig. 2 are reasonable and of the same order as measurements made at the twin tip with x-ray diffraction techniques (Ref 13). Along line A-B, the  $\varepsilon_{yy}^e$  component is tensile up to 0.2% on the left side of the twin tip and compressive strains up to 0.25% on the right side.

The elastic strains are also measured inside the twin domain using a diffraction pattern obtained from the center of the twin as a reference. The calculated elastic strain fields inside the twin domain are shown in Fig. 3. The strain field inside the twin domain is relatively small and homogeneous compared to the surrounding parent crystal. The observed low strain values result from the choice of reference point, which is taken from the same twin domain. The actual absolute elastic strain values, in other words, may be higher. The elastic strain profile along line C-D is plotted in Fig. 3d. Along line C-D,  $\varepsilon_{yy}^e$ , and  $\varepsilon_{xy}^e$  oscillate irregularly between  $\pm 0.5\%$ , while  $\varepsilon_{xx}^e$  is slightly compressive, with strains reaching -0.5%. Overall, the relative strains inside the twin are relatively homogenous and low, qualitatively consistent with observations from NBED techniques (Ref 18).

## 3.2 Calculated Elastic Strain and Stress Fields Associated with a Twin

Figure 4 presents the calculated elastic strain fields that develop from the twin and free surface relaxation. These elastic strain fields are the actual values, unlike in the experiment where the relative strains are obtained. We postulate that the calculated strain fields would be roughly equivalent to the measured *relative* strains for the following reasons. In the calculations, no macroscopic loading is imposed so that calculated elastic strain fields result only from the twins. In the experiment, the reference point is taken from the parent grain, which has an effect of macroscopic loading and not the twinning shear. Thus, the measured relative strain fields most likely developed from the twins and not from the macroscopic loading, making them synonymous with those calculated.

The elastic strain fields  $\varepsilon_{xx}^e$ ,  $\varepsilon_{yy}^e$ , and  $\varepsilon_{xy}^e$  inside the twin domain are shown in Fig. (4b-d), and those in the parent matrix in Fig. (4e-g). The predicted strain components  $\varepsilon_{yy}^e$  and  $\varepsilon_{xy}^e$  agree well with the experimentally observed values. A strain asymmetry for  $\varepsilon_{yy}^e$  can be seen, with tensile strains up to 0.03% on the left of the twin tip and compressive strains up to -0.04% on the right of the twin tip. The  $\varepsilon_{xy}^e$  component shows a large localization at the twin tip, which agrees with the experiment. The  $\varepsilon_{xx}^e$  strain component exhibits the largest discrepancy from the experimentally measured values. As shown in Fig. 4e, the  $\varepsilon_{xx}^e$  fields ahead of the twin tip are compressive and decreasing in a conical shape moving away from the twin tip.

To directly compare with the strains measured along a line crossing the twin tip, the calculated strains along the line A-B marked in Fig. 4e, are plotted in Fig. 4h. Along line A-B, the model predicts compressive  $e_{xx}^e$  strains on both sides of the twin tip, with slightly lower strains of  $\sim -0.005\%$  on the left side and -0.02% on the right side of the twin tip. However, the calculated  $e_{xx}^e$  fields are relatively low compared to the other strain components, and it is possible that dislocation structures near the twin tip could result in relatively higher measured strains. All the measured  $e_{xx}^e$ ,  $e_{yy}^e$ , and  $e_{xy}^e$  strain components, seen in Fig. 2, extend as a diagonal band, which likely developed due to external loading, deformation history not accounted for in simulation.

Compared to the experimentally measured strains, the calculated  $\varepsilon_{xx}^e$ ,  $\varepsilon_{yy}^e$ , and  $\varepsilon_{xy}^e$  strain components are more uniform inside the twin, as seen in Fig. 4b-d. For a closer view, Fig. 4i plots these components along the line C-D. As shown, the model predicts that  $\varepsilon_{xx}^e$  is positive, and  $\varepsilon_{yy}^e$  and  $\varepsilon_{xy}^e$  are negative. However, the measured  $\varepsilon_{xx}^e$  is negative, while both  $\varepsilon_{yy}^e$  and  $\varepsilon_{xy}^e$  and eximinate in sign. The discrepancy in strain inside the twin domain could be due to the simplified model geometry used for the remaining twin domain outside of the STEM micrograph. Also, the oscillations in the  $\varepsilon_{yy}^e$  and  $\varepsilon_{xy}^e$  components could be due to the presence of dislocations that cut across the twins, as seen in Fig. 1a.

In addition to the elastic strains, the EVP-FFT model predicts all components of the stress tensor. The calculated distributions of stress components  $\sigma_{xx}$ ,  $\sigma_{yy}$ , and  $\sigma_{xy}$  are shown in Fig. 5a-c, respectively. The out-of-plane stress components,  $\sigma_{zz}$ ,  $\sigma_{vz}$ , and  $\sigma_{xz}$ , are nearly zero everywhere, as expected from the free surface relaxation boundary conditions we imposed. The calculated nonzero stresses are within reasonable limits of Mg and of the similar range as those measured by x-ray diffraction techniques (Ref 14). Additionally, the twin plane resolved shear stresses (TRSS) are calculated by resolving the stress tensor at each material point on the crystallographic twin plane and along the twinning shear direction. Figure 5d presents the TRSS map around the twin structure. Any positive TRSS value is a potential driving stress for the development of the twin. It can be observed in Fig. 5d that a positive TRSS concentrated at the tip of the twin in a conical shape with the line of height that is rotated counterclockwise from the vertical by approximately 23°. This driving stress is nearly symmetrically aligned about the twinning shear direction and favorable for propagation in the direction along the long dimension of the twin.

#### 3.3 Local Defects Near the Twin Domain

The analysis, thus far, indicates that the asymmetric shape of the twin tip generates an asymmetric stress/strain field in the surrounding parent crystal ahead of it. The magnitudes of these stresses are sufficiently intense to be accommodated by plasticity. It is anticipated that the resulting distributions of dislocations would be heterogeneous as well. Figure 6a-c shows the calculated total dislocation density per slip mode. The dark blue regions correspond to the initial dislocation density. Prismatic and pyramidal I type dislocations can be seen at the twin tip and locally around some regions of the twin boundary; however, they mainly develop within the twin domain itself. Basal dislocation density accumulates both within the twin and in the parent matrix far away from the twin. However, band of concentrated dislocation density can be observed emanating from the twin tip at an angle approximately

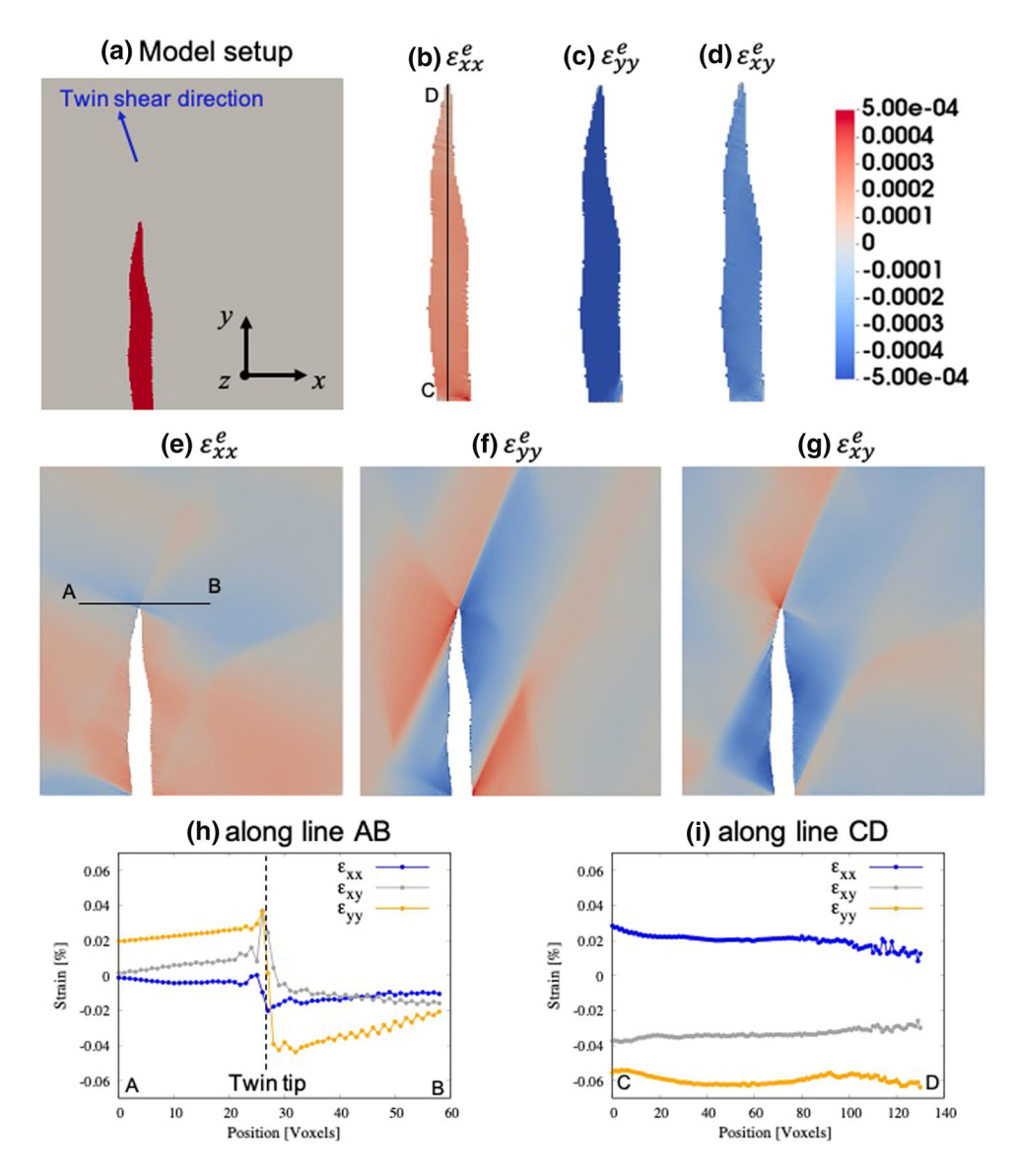


**Fig. 4** (a) EVP-FFT model setup for calculating fields around twin-2 shown in Fig. 1. Calculated elastic strains of (a) and (e)  $\varepsilon_{xx}^e$ , (b) and (f)  $\varepsilon_{yy}^e$ , and (c) and (g)  $\varepsilon_{xy}^e$  components inside and around the twin domain. Elastic strain profile along (h) line A-B (marked in (e)) ahead of the twin tip, and (i) line C-D (marked in (b)) inside the twin

30° clockwise from the vertical direction. The calculated dislocation distributions are consistent with the observed dislocation arrays that can be seen emanating from the twin tip in the STEM micrographs, see in Fig. 6d, as well as in other studies (Ref 21, 44-46).

## 3.4 Influence of Closely Spaced Neighboring Twins

Up to now, we analyzed the micromechanical fields that are generated ahead of a twin tip assuming the twin was isolated. However, the actual microstructure shown in Fig. 1 contains many nearby parallel twins that may influence the measured elastic strains (Ref 26, 47, 48). To determine the extent at which neighboring twins can influence strains that develop around a single twin, an additional simulation was performed, wherein which all five twin domains seen in the STEM micrograph were

modeled, as illustrated in Fig. 7a. The resulting strain fields are shown in Fig. 7c-e. Figure 7b presents the  $\varepsilon_{xx}^e$ ,  $\varepsilon_{yy}^e$ , and  $\varepsilon_{xy}^e$  strain components measured along line A-B, as marked in Fig. 7a. These components are remarkably like those in the isolated twin case, presented in Fig. 2h. The strain asymmetry across the twin tip is still observed for  $\varepsilon_{vv}^e$ , with tensile strains reaching 0.045% on the left side of the twin and compressive strains reaching -0.04% on the right side. The  $\varepsilon_{xy}^e$  component exhibits a comparable concentration at the twin tip, reaching shear strains of  $\sim 0.04\%$ . Lastly,  $\varepsilon_{xx}^e$  along line A-B is tensile and nearly homogenous. Previously, it was noted that  $\varepsilon_{xx}^e$  along the line A-B in the single twin was compressive. However, due to the fields of the nearby twins,  $\varepsilon_{xx}^e$  increases slightly by  $\sim 0.01\%$ becoming tensile across the twin tip, more consistent with experimentally measured values. Evidently, the neighboring twins affect the strain fields at the twin tip, although minimally.

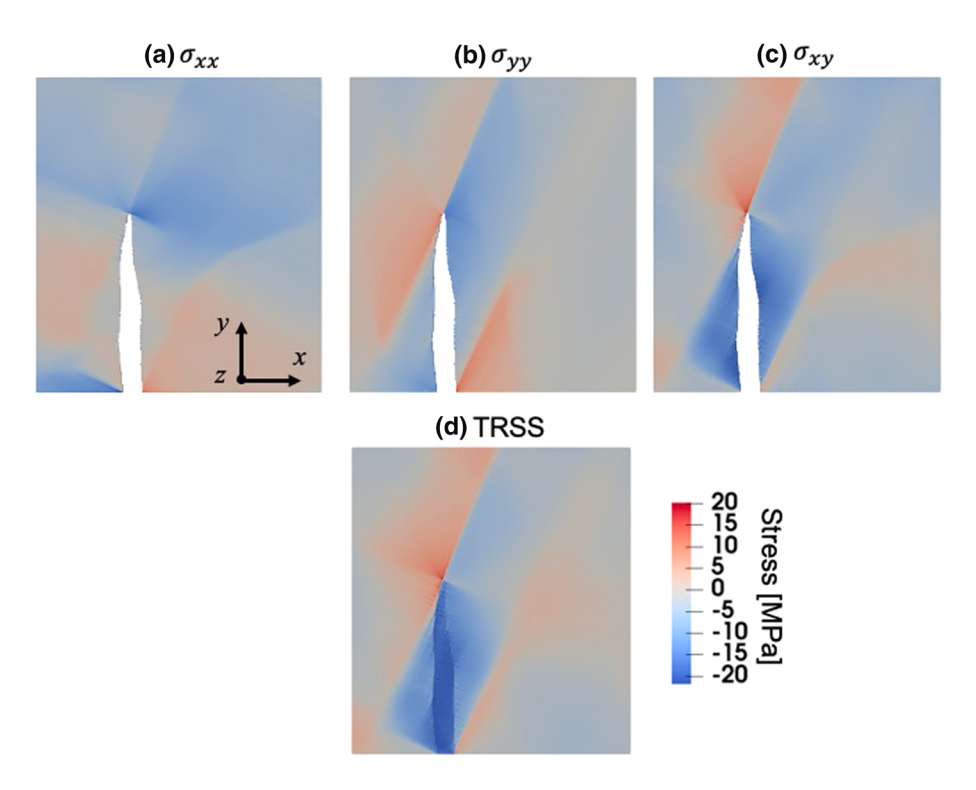


Fig. 5 Calculated (a)  $\sigma_{xx}$ , (b)  $\sigma_{yy}$ , and (c)  $\sigma_{xy}$  fields around the twin tip. (d) Distribution of twin-plane resolved shear stress (TRSS) within and outside the twin domain. Out-of-plane stress components are nearly zero due to the free surface (Ref 34)

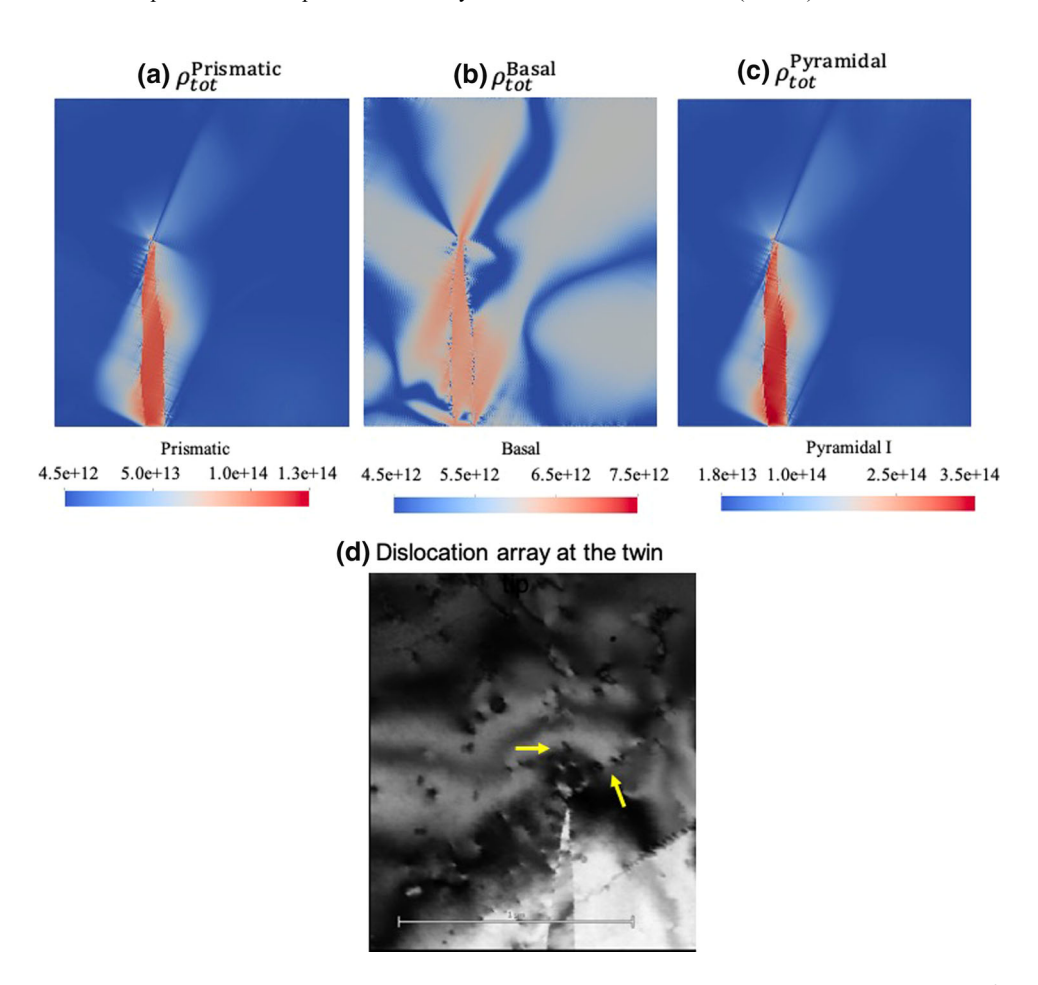


Fig. 6 Calculated distributions of twin-induced (a) prismatic, (b) basal, and (c) pyramidal slip dislocation density (in  $m^{-2}$ ) within and outside the twin domain. (d) STEM image shows the presence of dislocation arrays emitted at the twin tip

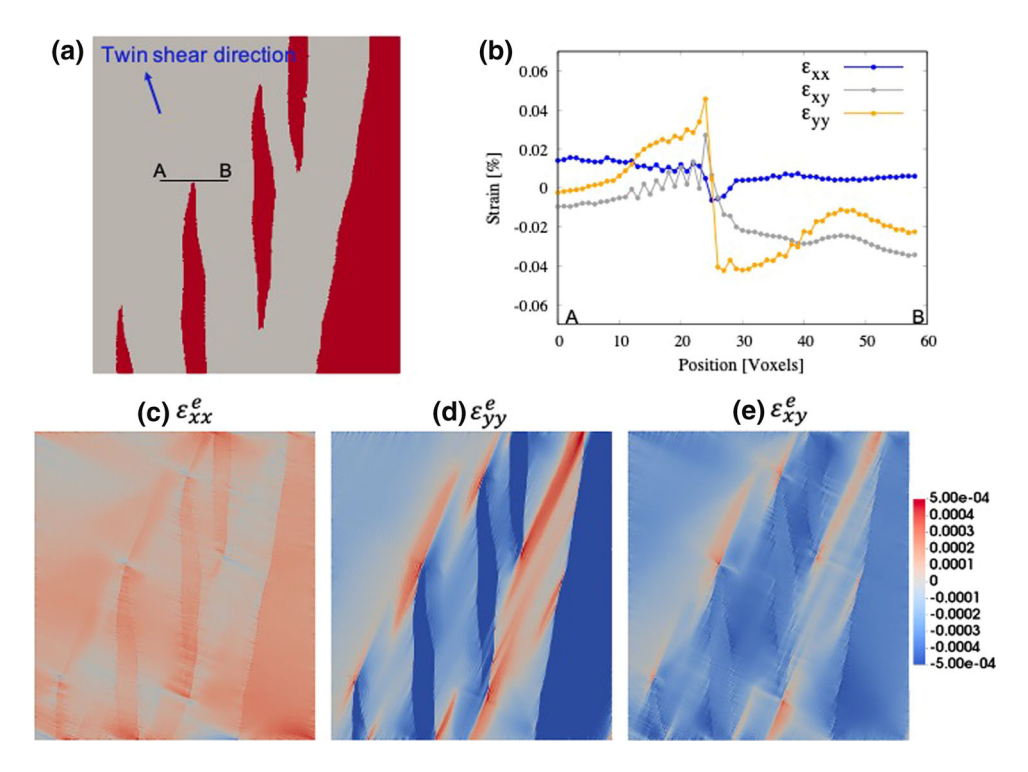


Fig. 7 Influence of nearby parallel twins on the elastic strain fields at the twin tip. (a) EVP-FFT model setup comprised of all five twin domains. (b) Calculated elastic strain profiles along line A-B ahead of twin-2. Spatial distribution of (c)  $\varepsilon_{xx}^e$ , (d)  $\varepsilon_{yy}^e$ , and (e)  $\varepsilon_{xy}^e$  fields with all five twins

## 3.5 Twin Morphology Versus Twin Shear Direction

As seen in Fig. 4, twin boundaries tend to be asymmetric and wavy, and as mentioned earlier, this morphology is common for HCP twins. The twins studied here, for instance in Fig. 4a, are asymmetric and the apparent twin propagation direction (i.e., the direction of the longest dimension of the twin) is skewed from the twinning shear direction. Yet, to date, whether the geometry of the twin tip has any effect on its continued propagation has not been systematically studied.

To investigate the geometric effects of twins on their propagation, three hypothetical configurations are considered. Figure 8 shows all three configurations and the model calculated respective strain fields. In Fig. 8a-c, the same crystallographic orientation of the parent matrix is considered, as seen in Fig. 4, and thus the twinning shear direction is the same, but the twin morphology is idealized to be symmetric. Next, in Fig. 8d-f, the irregular twin morphology is preserved, but the crystallographic orientation of parent matrix is selected so that the twinning shear direction is now parallel to the longest dimension of the twin. Last, in Fig. 8g-i, the twin morphology is symmetric and the twinning shear direction aligned with the twin long dimension.

Figure 8 compares the strain fields for all three cases. Interestingly, the resulting elastic strain fields are remarkably similar to those seen in Fig. 4e-g. The only notable difference lies in the distribution of  $\varepsilon_{xx}^e$  along the lateral sides of the twin in the symmetrically shaped twin compared to the original irregular twin. Furthermore, the elastic strain fields in Fig. 8d-f and Fig. 8g-i are nearly identical, although they clearly differ from the actual twin configuration shown in Fig. 4. These results imply that the twin geometry plays a

relatively minor role on the distributions of the micromechanical fields, whereas the twinning shear direction has a greater influence on the measured micromechanical fields around a twin.

## 4. Summary

In this work, the elastic strain fields within and around  $\{10\overline{1}2\}$  tensile twins in AZ31B magnesium alloy are characterized. The elastic strain fields are measured using the nanoprecision electron diffraction (N-PED) technique. Unlike other nm resolution elastic strain measurement techniques, like nanobeam electron diffraction (NBEB), the measured strains values using the N-PED technique are realistic and within the elastic limit of the material. Also, the measured elastic strain values are very similar to those obtained using in-situ x-ray synchrotron techniques. Explicit simulation of deformation twinning using an EVP-FFT framework along with the free surface relaxation process correctly captures the experimentally measured heterogenicity in the elastic strain fields. Apart from the elastic strain fields, the EVP-FFT model also provides the dislocation density and stress fields, which are not easily obtainable from the experiment. The model was then used to elucidate the effects of nearby twins and the twin geometry on the development of elastic strains ahead of twin and within the twin. The simulation results reveal that the nearby twins weakly influence elastic strains around and inside a twin. As the final important finding, it is shown that the twinning shear direction is the major contributor to the observed micromechanical fields

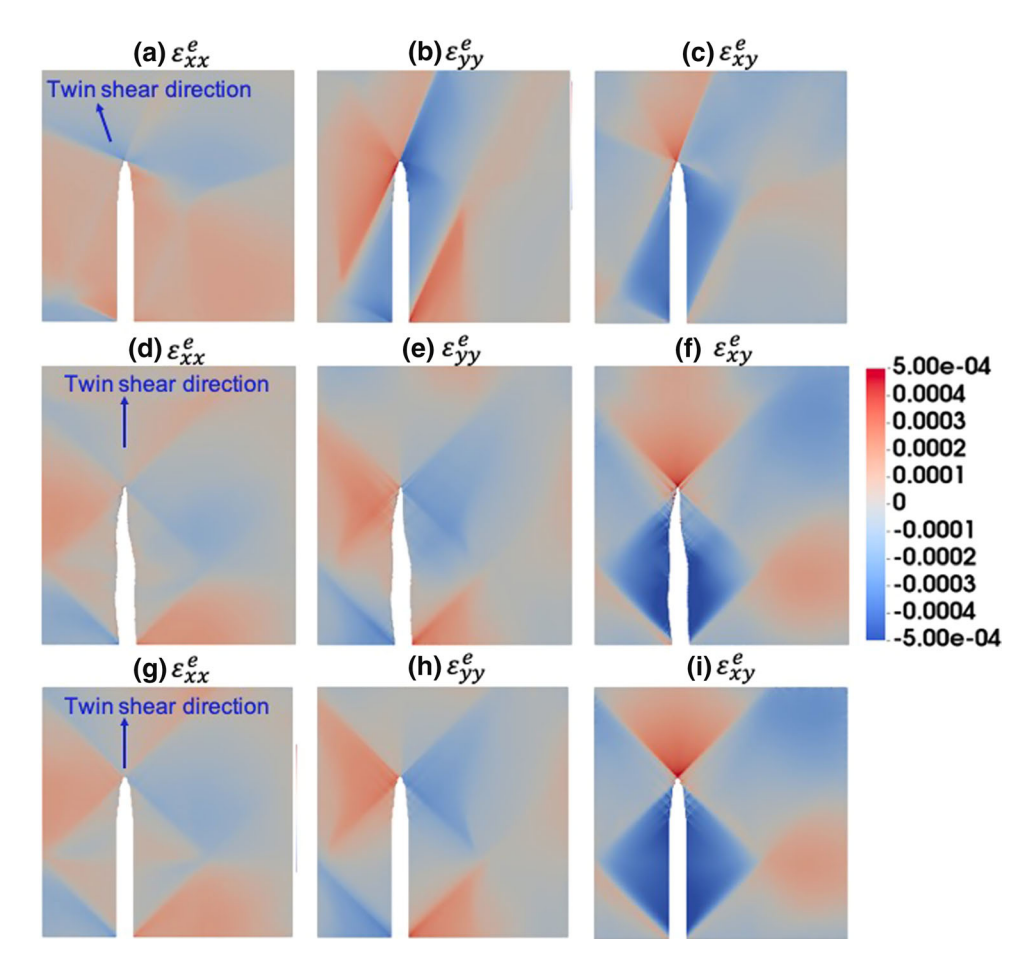


Fig. 8 Effect of twin morphology and shear direction on the micromechanical fields associated with the twin. First row: symmetric twin morphology with actual twinning shear direction; second and third row: actual irregular and symmetric twin morphology with the shear direction parallel to the long dimension of the twin. The first, second, and third columns correspond to elastic strains  $\varepsilon_{xx}^e$ ,  $\varepsilon_{yy}^e$ , and  $\varepsilon_{xy}^e$ , respectively

that arise due to the formation of the twin, and the shape of the twin domain has little consequence.

## **Acknowledgments**

The authors acknowledge financial support from the National Science Foundation, B. L. and I.J.B. for NSF MOM-2051390 and K.J.H for NSF DMR-1709865. M.A.K acknowledges financial support from the US Dept. of Energy, Office of Basic Energy Sciences Project FWP 06SCPE401. The authors thank Luoning Ma (Johns Hopkins University) for preparation of TEM specimen.

**Conflict of interest** The authors declare no conflict of interest.

#### **Open Access**

This article is licensed under a Creative Commons Attribution 4.0 International License, which permits use, sharing, adaptation, distribution and reproduction in any medium or format, as long as you give appropriate credit to the original author(s) and the source, provide a link to the Creative Commons licence, and indicate if changes were made. The images or other third party material in this article are included in the article's Creative Commons licence, unless indicated otherwise in a credit line to the material. If material is not included in the article's Creative Commons licence and your intended use is not permitted by statutory regulation or

exceeds the permitted use, you will need to obtain permission directly from the copyright holder. To view a copy of this licence, visit http://creativecommons.org/licenses/by/4.0/.

#### References

- M.H. Yoo, and J.K. Lee, Deformation Twinning in h.c.p. Metals and Alloys, *Philos. Mag. A Phys. Condens. Matter. Struct. Defects Mech. Prop.*, 1991, 63, p 987–1000. https://doi.org/10.1080/ 01418619108213931
- J.W. Christian, and S. Mahajan, Deformation Twinning, Prog. Mater. Sci., 1995, 39, p 1–157. https://doi.org/10.1016/0079-6425(94)00007-7
- J. Wang, S.K. Yadav, J.P. Hirth, C.N. Tomé, and I.J. Beyerlein, Pure-Shuffle Nucleation of Deformation Twins in Hexagonal-Close-Packed Metals, *Mater. Res. Lett.*, 2013, 1, p 126–132. https://doi.org/10.1080/21663831.2013.792019
- I.J. Beyerlein, L. Capolungo, P.E. Marshall, R.J. McCabe, and C.N. Tome, Statistical Analyses of Deformation Twinning in Magnesium, *Philos. Mag.*, 2010, 90, p 2161–2190. https://doi.org/10.1080/ 14786431003630835
- Y. Hu, V. Turlo, I.J. Beyerlein, S. Mahajan, E.J. Lavernia, J.M. Schoenung, and T.J. Rupert, Disconnection-Mediated Twin Embryo Growth in Mg, *Acta Mater.*, 2020, 194, p 437–451. https://doi.org/10.1016/j.actamat.2020.04.010
- M.A. Kumar, and I.J. Beyerlein, Local Microstructure and Micromechanical Stress Evolution During Deformation Twinning in Hexagonal Polycrystals, J. Mater. Res., 2020 https://doi.org/10.1557/jmr.2020.14
- J. Wang, I.J. Beyerlein, and C.N. Tomé, Reactions of Lattice Dislocations with Grain Boundaries in Mg: Implications on the Micro

- Scale from Atomic-Scale Calculations, *Int. J. Plast.*, 2014, **56**, p 156–172. https://doi.org/10.1016/j.ijplas.2013.11.009
- J. Wang, L. Liu, C.N. Tomé, S.X. Mao, and S.K. Gong, Twinning and De-twinning Via Glide and Climb of Twinning Dislocations Along Serrated Coherent Twin Boundaries in Hexagonal-Close-Packed Metals, *Mater. Res. Lett.*, 2013, 1, p 81–88. https://doi.org/10.1080/ 21663831.2013.779601
- A. Ostapovets, and R. Gröger, Twinning Disconnections and Basal-Prismatic Twin Boundary in Magnesium, *Model. Simul. Mater. Sci. Eng.*, 2014 https://doi.org/10.1088/0965-0393/22/2/025015
- M. Gong, J.P. Hirth, Y. Liu, Y. Shen, and J. Wang, Interface Structures and Twinning Mechanisms of Twins in Hexagonal Metals, *Mater. Res. Lett.*, 2017, 5, p 449–464. https://doi.org/10.1080/ 21663831.2017.1336496
- M.A. Kumar, I.J. Beyerlein, R.A. Lebensohn, and C.N. Tomé, Role of Alloying Elements on Twin Growth and Twin Transmission in Magnesium Alloys, *Mater. Sci. Eng. A.*, 2017, 706, p 295–303. https://doi.org/10.1016/j.msea.2017.08.084
- I. Basu, H. Fidder, V. Ocelík, J.T.M. De Hosson, and J.T.M. de Hosson, Local Stress States and Microstructural Damage Response Associated with Deformation Twins in Hexagonal Close Packed Metals, *Crystals.*, 2017, 8, p. 1. https://doi.org/10.3390/cryst8010001
- L. Balogh, S.R. Niezgoda, A.K. Kanjarla, D.W. Brown, B. Clausen, W. Liu, and C.N. Tomé, Spatially Resolved In Situ Strain Measurements from an Interior Twinned Grain in Bulk Polycrystalline AZ31 Alloy, *Acta Mater.*, 2013, 61, p 3612–3620. https://doi.org/10.1016/j.actamat.2013.02.048
- C.C. Aydiner, J.V. Bernier, B. Clausen, U. Lienert, C.N. Tomé, and D. W. Brown, Evolution of Stress in Individual Grains and Twins in a Magnesium Alloy Aggregate, *Phys. Rev. B.*, 2009, 80, p 1–6. https://doi.org/10.1103/PhysRevB.80.024113
- S.R. Kalidindi, A.A. Salem, and R.D. Doherty, Role of Deformation Twinning on Strain Hardening in Cubic and Hexagonal Polycrystalline Metals, Adv. Eng. Mater., 2003, 5, p 229–232. https://doi.org/10.1002/adem.200300320
- W.Z. Han, J.S. Carpenter, J. Wang, I.J. Beyerlein, and N.A. Mara, Atomic-Level Study of Twin Nucleation from Face-Centered-Cubic/ Body- Centered-Cubic interfaces in Nanolamellar Composites, *Appl. Phys. Lett.*, 2012, 100, p 554. https://doi.org/10.1063/1.3675447
- K. Dang, S. Wang, M. Gong, R.J. McCabe, J. Wang, and L. Capolungo, Formation and Stability of Long Basal-Prismatic Facets in Mg, *Acta Mater.*, 2020, 185, p 119–128. https://doi.org/10.1016/j.actamat.2019.11.070
- J.S. Chen, Y. Liu, R.J. McCabe, J. Wang, and C.N. Tomé, Quantifying Elastic Strain Near Coherent Twin Interface in Magnesium with Nanometric Resolution, *Mater. Charact.*, 2020, 160, p 110082. https://doi.org/10.1016/j.matchar.2019.110082
- L. Ma, P.F. Rottmann, K. Xie, and K.J. Hemker, Nano-Scale Elastic Strain Maps of Twins in Magnesium Alloys, *Microsc. Microanal.*, 2018, 24, p 970–971. https://doi.org/10.1017/s1431927618005342
- P.F. Rottmann, and K.J. Hemker, Nanoscale Elastic Strain Mapping of Polycrystalline Materials, *Mater. Res. Lett.*, 2018, 6, p 249–254. https://doi.org/10.1080/21663831.2018.1436609
- K. Yaddanapudi, B. Leu, M.A. Kumar, X. Wang, J.M. Schoenung, E.J. Lavernia, T.J. Rupert, I.J. Beyerlein, and S. Mahajan, Accommodation and Formation of 1012 Twins in Mg-Y Alloys, *Acta Mater.*, 2021, 204, p 116514. https://doi.org/10.1016/j.actamat.2020.116514
- S.G. Song, and G.T. Gray, Structural Interpretation of the Nucleation and Growth of Deformation Tem Study of Twin Morphology and Defect Reactions During Twinning, *Acta Metall. Mater.*, 1995, 43, p 2339–2350. https://doi.org/10.1016/0956-7151(94)00434-X
- J.Tu.Zhang, ZM.Zhou,C. HuangStructural characterization of {10 1<sup>-2</sup>} twin tipin deformed magnesium alloy, 1995, 43, p 2339–2350. https://doi.org/10.1016/0956-7151(94)00434-X
- V. Livescu, I.J. Beyerlein, C.A. Bronkhorst, O.F. Dippo, B.G. Ndefru, L. Capolungo, and H.M. Mourad, Microstructure insenSitive Twinning: A Statistical Analysis of Incipient Twins in High-Purity Titanium, *Materialia.*, 2019, 6, p 100303. https://doi.org/10.1016/j.mtla.2019.100303
- R.A. Lebensohn, A.K. Kanjarla, and P. Eisenlohr, An Elasto-Viscoplastic Formulation Based on Fast Fourier Transforms for the Prediction of Micromechanical Fields in Polycrystalline Materials, *Int. J. Plast.*, 2012, 32–33, p 59–69. https://doi.org/10.1016/j.ijplas.2011.12.005
- M. A. Kumar, B. Leu, P. Rottmann, I.J. Beyerlein, Characterization of Staggered Twin Formation in HCP Magnesium, in: TMS Magnes.

- Technol. 2019, TMS, 2019: pp. 207–213. https://doi.org/10.1007/978-3-030-05789-3 17
- H. Wang, B. Clausen, L. Capolungo, I.J. Beyerlein, J. Wang, and C.N. Tomé, Stress and Strain Relaxation in Magnesium AZ31 Rolled Plate: In-situ Neutron Measurement and Elastic Viscoplastic Polycrystal Modeling, Int. J. Plast., 2016, 79, p 275–292. https://doi.org/10.1016/j.ijplas.2015.07.004
- L. Capolungo, R.J. Mccabe, W. Liu, J.Z. Tischler, and C.N. Tomé, Deformation Twinning and Grain Partitioning in a Hexagonal Close-Packed Magnesium Alloy, *Nat. Commun.*, 2011 https://doi.org/ 10.1038/s41467-018-07028-w
- E.F. Rauch, and M. Veron, Coupled Microstructural Observations and Local Texture Measurements with an Automated Crystallographic Orientation Mapping Tool Attached to a Tem, *Materwiss. Werksttech.*, 2005, 36, p 552–556. https://doi.org/10.1002/mawe.200500923
- M.A. Kumar, A.K. Kanjarla, S.R. Niezgoda, R.A. Lebensohn, and C. N. Tomé, Numerical Study of the Stress State of a Deformation Twin in Magnesium, *Acta Mater.*, 2015, 84, p 349–358. https://doi.org/10.1016/j.actamat.2014.10.048
- B. Leu, M. Arul Kumar, I.J. Beyerlein, The Effects of Basal and Prismatic Precipitates on Deformation Twinning in AZ91 Magnesium Alloy, in: TMS Magnes. Technol. 2021, TMS, 2021: pp. 73–79
- B. Anthony, B. Leu, I.J. Beyerlein, and V.M. Miller, Deformation Twin Interactions with Grain Boundary Particles in Multi-Phase Magnesium alloys, *Acta Mater.*, 2021, 219, p 117225. https://doi.org/10.1016/j. actamat.2021.117225
- M.A. Kumar, L. Capolungo, R.J. McCabe, and C.N. Tomé, Characterizing the Role of Adjoining Twins at Grain Boundaries in Hexagonal Close Packed Materials, *Sci. Rep.*, 2019, 9, p 1–10. https://doi.org/10.1038/s41598-019-40615-5
- B. Leu, M.A. Kumar, and I.J. Beyerlein, The Effects of Free Surfaces on Deformation Twinning in HCP Metals, *Materialia*., 2021, 17, p 101124. https://doi.org/10.1016/j.mtla.2021.101124
- I.J. Beyerlein, and C.N. Tomé, A dislocation-based constitutive law for pure Zr including temperature effects, *Int. J. Plast.*, 2008, 24, p 867– 895. https://doi.org/10.1016/j.ijplas.2007.07.017
- R. Madec, B. Devincre, and L.P. Kubin, From Dislocation Junctions to Forest Hardening, *Phys. Rev. Lett.*, 2002, 89, p 1–4. https://doi.org/ 10.1103/PhysRevLett.89.255508
- L. Capolungo, I.J. Beyerlein, and C.N. Tomé, Slip-Assisted Twin Growth in Hexagonal Close-Packed Metals, Scr. Mater., 2009, 60, p 32–35. https://doi.org/10.1016/j.scriptamat.2008.08.044
- 38. F.F. Lavrentev, and Y.A. Pokhil, Effect of Forest Dislocations in the 1122 □1123□ System on Hardening in Mg Single Crystals Under Basal slip, *Phys. Status Solidi.*, 1975, **32**, p 227–232. https://doi.org/10.1002/pssa.2210320125
- P. Franciosi, and A. Zaoui, Multislip in f.c.c. Crystals a Theoretical Approach Compared with Experimental Data, *Acta Metall.*, 1982, 30, p 1627–1637. https://doi.org/10.1016/0001-6160(82)90184-5
- U.F. Kocks, and H. Mecking, Physics and Phenomenology of Strain Hardening: The FCC Case, *Prog. Mater. Sci.*, 2003, 48, p 172–268. https://doi.org/10.4324/9781315279015
- M. Lentz, M. Klaus, M. Wagner, C. Fahrenson, I.J. Beyerlein, M. Zecevic, W. Reimers, and M. Knezevic, Effect of Age Hardening on the Deformation Behavior of an Mg-Y-Nd Alloy: In-situ X-ray Diffraction and Crystal Plasticity Modeling, *Mater. Sci. Eng. A.*, 2015, 628, p 396–409. https://doi.org/10.1016/j.msea.2015.01.069
- 42. G. Simmons, and H. Wang, Single Crystal Elastic Constants and Calculated Aggregate Progress, 2nd ed. M.I.T. Press, London, 1965
- I.J. Beyerlein, R.J. Mccabe, and C.N. Tome, Effect of Microstructure on the Nucleation of Deformation Twins in Polycrystalline High-Purity Magnesium: A Multi-scale Modeling Study, *J. Mech. Phys. Solids.*, 2011, 59, p 988–1003. https://doi.org/10.1016/j.jmps.2011.02.007
- 44. L. Jiang, M.A. Kumar, I.J. Beyerlein, X. Wang, D. Zhang, C. Wu, C. Cooper, T.J. Rupert, S. Mahajan, E.J. Lavernia, and J.M. Schoenung, Twin Formation from a Twin Boundary in Mg During In-situ Nanomechanical Testing, *Mater. Sci. Eng. A.*, 2019, 759, p 142–153. https://doi.org/10.1016/j.msea.2019.04.117
- Y. Minonishi, S. Morozumi, and H. Yoshinaga, Accommodation Around 1011 Twins in Titanium, *Scr. Metall.*, 1985, 19, p 1241–1245. https://doi.org/10.1016/0036-9748(85)90246-7
- 46. E. Roberts, and P.G. Partridge, The Accommodation Around 1012 □1011□ Twins in Magnesium, *Acta Metall.*, 1966, **14**, p 513–527. https://doi.org/10.1016/0001-6160(66)90319-1

- M. Gong, S. Xu, Y. Jiang, Y. Liu, and J. Wang, Structural Characteristics of 1012 Non-cozone Twin-Twin Interactions in Magnesium, *Acta Mater.*, 2018, 159, p 65–76. https://doi.org/10.1016/j.actamat.2018.08.004
- 48. M.A. Kumar, M. Gong, I.J. Beyerlein, J. Wang, and C.N. Tomé, Role of Local Stresses on Co-zone Twin-Twin Junction Formation in HCP

Magnesium, *Acta Mater.*, 2019, **168**, p 353–361. https://doi.org/10.1016/j.actamat.2019.02.037

**Publisher's Note** Springer Nature remains neutral with regard to jurisdictional claims in published maps and institutional affiliations